

An Earth-mass planet and a brown dwarf in orbit around a white dwarf

Received: 15 March 2024

Accepted: 30 August 2024

Published online: 26 September 2024

 Check for updates

Keming Zhang  ^{1,2,3}, Weicheng Zang  ^{4,5}, Kareem El-Badry⁶, Jessica R. Lu  ³, Joshua S. Bloom³, Eric Agol  ⁷, B. Scott Gaudi  ⁸, Quinn Konopacky  ¹, Natalie LeBaron  ³, Shude Mao  ⁴ & Sean Terry^{3,9,10}

It has been theorized that terrestrial planets born beyond 1–3 au could avoid being engulfed during the red-giant phases of their host stars.

Nevertheless, only a few gas-giant planets have been observed around white dwarfs (WDs), the end product left behind by a red giant. Here we report on evidence that the lens system that produced the microlensing event KMT-2020-BLG-0414 is composed of a WD orbited by an Earth-mass planet and a brown dwarf companion, as shown by the non-detection of the lens flux using Keck adaptive optics. From microlensing orbital motion constraints, we determine the planet to be a 1.9 ± 0.2 Earth-mass (M_{\oplus}) planet at a physical separation of 2.1 ± 0.2 au from the WD during the event. By considering the system's evolutionary history, we determine the brown dwarf companion to have a projected separation of 22 au from the WD and reject a degenerate model that places the brown dwarf at 0.2 au. Given the planetary orbital expansion during the final evolutionary stages of the host star, this Earth-mass planet may have existed in an initial orbit close to 1 au, thereby offering a glimpse into the possible survival of planet Earth in the distant future.

The ultra-high-magnification nature of the microlensing event KMT-2020-BLG-0414 (KB200414 hereafter) has previously prompted intensive photometric follow-up observations around the peak of the event on 11 July 2020. Modelling of the densely sampled light curve subsequently revealed a three-body lens system consisting of a low-mass-ratio planet ($q \approx 10^{-5}$) and a brown dwarf (BD) companion orbiting a subsolar-mass host star¹. Owing to intrinsic microlensing degeneracies^{2–4}, four distinct models explain the light-curve data equally well. Among the four models, the projected separation for the BD companion could be very close (~0.2 au) or very wide (~20 au), and the relative proper motion of the lens and source could be either in the north-east (NE) or south-east (SE) directions, which are associated

with distinct microlensing parallax constraints. On the other hand, the planet properties are consistent across the four models, all of which indicate an approximately Earth-mass planet at a projected separation of around 1–2 au.

For KB200414, the mass of the primary lens star (Table 1), as inferred from the finite-source effects and microlensing parallax, indicates that it is either a main-sequence (MS) star or a white dwarf (WD) stellar remnant. An MS lens star would be expected to have a similar apparent brightness as the microlensing source star, whose apparent brightness is known from the magnification profile. On the other hand, a WD lens would be expected to be fainter by 6–8 mag, making it practically undetectable under the glare of the source star.

¹Department of Astronomy and Astrophysics, University of California, San Diego, San Diego, CA, USA. ²Halıcıoğlu Data Science Institute, University of California, San Diego, San Diego, CA, USA. ³Department of Astronomy, University of California, Berkeley, Berkeley, CA, USA. ⁴Department of Astronomy, Tsinghua University, Beijing, China. ⁵Center for Astrophysics, Harvard & Smithsonian, Cambridge, MA, USA. ⁶Department of Astronomy, California Institute of Technology, Pasadena, CA, USA. ⁷Department of Astronomy, University of Washington, Seattle, WA, USA. ⁸Department of Astronomy, The Ohio State University, Columbus, OH, USA. ⁹Department of Astronomy, University of Maryland, College Park, MD, USA. ¹⁰NASA Goddard Space Flight Center, Greenbelt, MD, USA.  e-mail: kemingz@berkeley.edu; weicheng.zang@cfa.harvard.edu

Table 1 | Properties of the lens system KMT-2020-BLG-0414L(bc) under a fourfold light-curve degeneracy, with a uniform Bayesian prior

Parameter	Unit	North-east		South-east	
		Close	Wide	Close	Wide
Primary lens mass	M_{\odot}	$0.45^{+0.10}_{-0.08}$	$0.36^{+0.08}_{-0.06}$	$0.25^{+0.06}_{-0.03}$	$0.19^{+0.06}_{-0.04}$
Distance	kpc	$1.12^{+0.23}_{-0.19}$	$0.99^{+0.20}_{-0.17}$	$0.73^{+0.15}_{-0.09}$	$0.57^{+0.14}_{-0.09}$
Minimum MS lens brightness (K_s)	mag	$16.32^{+0.27}_{-0.26}$	$16.84^{+0.24}_{-0.34}$	$17.16^{+0.16}_{-0.18}$	$17.25^{+0.16}_{-0.19}$
Einstein radius	mas	$1.73^{+0.06}_{-0.06}$	$1.65^{+0.07}_{-0.06}$	$1.62^{+0.05}_{-0.04}$	$1.64^{+0.05}_{-0.04}$
Microlensing parallax	–	$0.45^{+0.10}_{-0.08}$	$0.54^{+0.12}_{-0.10}$	$0.76^{+0.12}_{-0.15}$	$0.99^{+0.21}_{-0.22}$
Source brightness (K_s)	mag	17.08 ± 0.06	16.99 ± 0.06	17.03 ± 0.06	16.95 ± 0.06
3σ excess brightness (K_s)	mag	18.63	19.06	18.88	19.34

North-east and south-east indicate the direction of the relative proper motion of the lens and source, which corresponds to the $u_0 > 0$ and $u_0 < 0$ solutions under the ecliptic degeneracy^{3,4}. Close and wide relate to the projected separation of the BD. Reported values are median values with 68% confidence intervals. The minimum MS lens brightness is defined as the minimum brightness for metal-rich ([Fe/H]=0.5) stars aged over 100 Myr to 10 Gyr. The microlensing parallax is the ratio between the lens–source relative parallax and the angular Einstein radius. The 3σ excess flux is the upper limit of the excess flux at 99.7% (3σ) confidence, defined as the difference between the observed flux ($K_s = 16.99 \pm 0.03$) and the source flux.

Therefore, the two scenarios could be distinguished by measuring the total brightness at the event location before or after the event. OGLE-III pre-event imaging (Fig. 1a) measured the total brightness at the event location to be $I_{\text{base}} = 18.46 \pm 0.09$, which implies a total blended flux of $I \approx 19.3$ on top of the unmagnified source star brightness of $I \approx 19.1$. This blended light was originally reported by ref. 1 as consistent with the expected MS lens brightness (Table 1) but could also be attributed to nearby field stars that cannot be resolved with seeing-limited imaging.

To further constrain the lens brightness, we observed the location of KB200414 in the K-short infrared passband (K_s ; 2.146 μm) with laser-guide-star adaptive optics^{5,6} on the Keck II telescope on 25 May 2023 (UT), approximately 3 yr after the peak of the event. Using our Keck images (Fig. 1c), we measured a total brightness of $K_s = 16.99 \pm 0.03$ at the event location within a circular aperture of radius 0.2", which closely matches the infrared source brightness, which ranges from $K_s = 16.95 \pm 0.06$ to 17.08 ± 0.06 , for the four degenerate solutions (Methods). Our high-angular-resolution imaging revealed that the blended light in OGLE-III pre-event imaging arose primarily from field stars within 0.5" to the west and north-west (Fig. 1). As shown in Table 1, our aperture photometry constrains any excess flux above the source flux to be at least around 2 mag fainter (at the 3σ level) than the expected brightness of the lens star, if it were on the MS. Therefore, we rejected the MS hypothesis and concluded that the primary lens star (the planet's host) must be a WD.

The conclusion that the primary lens is a WD called for a re-examination of the four degenerate light-curve models. We found that the two SE solutions are unlikely, as both would require an extremely low-mass (ELM) WD below $0.3 M_{\odot}$. ELM WDs (for example, refs. 7,8) are a rare class of WDs formed exclusively through binary interactions during which the companion star strips away the stellar envelope from the ELM WD progenitor through either common-envelope evolution or stable mass transfer before the progenitor star can initiate helium burning (for example, refs. 9,10). We immediately ruled out the existence of such massive companions to the lens star, as the light-curve models constrain the total lens mass as opposed to the primary lens mass for close-in binaries. It was also difficult to attribute the formation of an ELM WD to the close-in BD companion under the close SE model,

as binary evolutionary models^{11,12} predict that a BD companion could eject the envelope of the WD progenitor only if it spiralled in to a much closer orbit ($\lesssim 0.01$ au) or first interacted with the progenitor when it was an asymptotic giant branch (AGB) star whose core mass has grown to more than $\sim 0.5 M_{\odot}$.

On the other hand, the two NE models do not require the formation of an ELM WD in a compact binary. As the finite age of the Universe limits the lowest mass of a WD that can form due to the evolution of a single star, we imposed a host-mass lower limit of $M > 0.45 M_{\odot}$ based on WD population statistics (for example, refs. 13,14), which served as a Bayesian prior to refine the lens system's properties. Under this extra constraint, both the close NE and wide NE models indicate that there is an approximately 1.7 – $1.9 M_{\odot}$ planet at a projected separation of around 2.1 au with a host mass near $0.5 M_{\odot}$ (Table 2). The planet mass is consistent with a rocky composition, and the corresponding planet size would be merely 20% greater than Earth's radius from mass–radius relationships (for example, refs. 15,16). Furthermore, we inferred from WD initial–final mass relations¹⁷ that the progenitor (MS) mass was likely around 1–2 M_{\odot} .

We then inferred the planet's physical separation from its projected separation using the orbital-motion effect^{18,19} in the light-curve models (Extended Data Table 1 and Methods). We adopted a log-uniform prior on the physical separation and modelled the planet's orbit for different assumed eccentricities. As illustrated in Fig. 2, the posterior distribution for the physical separation is bimodal, which reflects two distinctly allowed orbital configurations (Extended Data Fig. 1). The planet is most probably near its greatest elongation in an inclined orbit, which implies that the physical separation is near the projected separation. Alternatively, the planet is near conjunction on a nearly edge-on orbit, which implies a physical separation of $\gtrsim 10$ au. The former scenario is substantially favoured for eccentricities up to $e < 0.2$, for which we could place an upper limit to the physical separation at 2.3 au with 80–90% confidence. Due to tidal circularization during the host star's red-giant phases (for example, refs. 20,21), we consider it reasonable to assume that the current planetary orbit indeed has low eccentricity.

For low eccentricities of $e < 0.2$, the greatest-elongation or close-orbit case ($d \approx 2.1$ au) is formally favoured by a Bayes factor of around 5–10, which constitutes only substantial but not strong evidence²². Therefore, the extent to which the conjunction or wide-orbit case ($d \gtrsim 10$ au) may be ruled out is sensitive to the adopted physical separation prior, which is complicated because the population of terrestrial planets at such separations remains largely unexplored. Canonical planet formation theory expects terrestrial planets to form predominantly within the water-ice line at around 3 au for a Sun-like star (for example, ref. 23). However, processes such as planet–planet gravitational interactions during the early stages of planet formation could scatter low-mass planets to very wide separations or outright eject them²⁴. Statistics from short-timescale microlensing events ($t_E \lesssim 0.5$ d) indicate that wide-orbit ($\gtrsim 10$ au) and free-floating low-mass planets combined are at least as abundant as the known population of close-orbit planets^{25,26}, but current follow-up observations are insufficient to distinguish between the two scenarios²⁷. Therefore, if a considerable fraction of such candidates for microlensing free-floating low-mass planets are confirmed to be bound planets (by direct detection of the host star), then it becomes more probable for the Earth-mass planet (KB200414Lb) to have a wider orbit than at present inferred.

Similarly (but for a different reason), the BD companion takes on either a very close or very wide projected separation, which would indicate distinct evolutionary histories (Fig. 3). To end up in a close-in orbit of $\gtrsim 0.2$ au under the close NE model, the BD companion would probably have gone through a period of common-envelope evolution with the WD progenitor and successfully ejected the stellar envelope. However, most known post-common-envelope binaries have orbits smaller than 0.01 au (ref. 28). Several WD binaries with MS companions are known with separations of order 0.2 au that are suspected to be

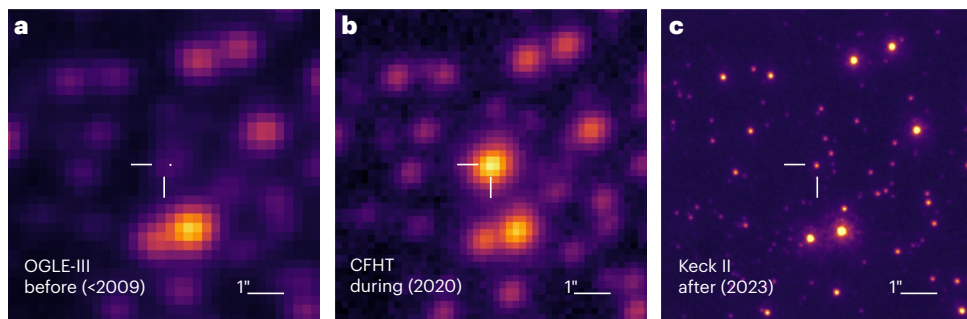


Fig. 1 | OGLE-III, CFHT and Keck II imaging of KMT-2020-BLG-0414 taken before, during and after the event. **a**, OGLE-III *I*-band image taken from 2002 to 2009. The event location is centred on the cross-hairs. The OGLE-III baseline (catalogue) object is 0.18" west and 0.01" south of the event location, as indicated

by the white dot. **b**, CFHT/MegaCam *I*-band image taken 2.2 d after the peak of the event. **c**, Keck adaptive optics K_s -band imaging reveals that the blend flux associated with the OGLE-III baseline object is predominantly attributed to field stars to the west or north-west within 0.5".

Table 2 | Refined properties of the WD planetary system KMT-2020-BLG-0414L under a host-mass limit of $M > 0.45 M_\odot$

Parameter	Unit	Close NE	Wide NE
WD mass	M_\odot	$0.51^{+0.08}_{-0.05}$	$0.49^{+0.06}_{-0.03}$
Distance	kpc	$1.27^{+0.19}_{-0.12}$	$1.33^{+0.16}_{-0.12}$
WD flux (K_s)	mag	$23.8^{+0.7}_{-0.6}$	$24.0^{+0.6}_{-0.8}$
Proper motion	mas yr^{-1}	$7.74^{+1.52}_{-0.63}$	$7.77^{+1.29}_{-0.76}$
Proper motion direction	deg	$62.9^{+21.4}_{-21.7}$	$68.5^{+15.4}_{-20.2}$
Planet mass	M_\oplus	$1.75^{+0.31}_{-0.18}$	$1.87^{+0.27}_{-0.16}$
Planet projected separation	au	$2.17^{+0.30}_{-0.17}$	$2.07^{+0.22}_{-0.11}$
Planet physical separation ($e < 0.2$)	au	$\gtrsim 10$	$2.07^{+0.24}_{-0.09}$
BD mass	M_J	$32.4^{+4.8}_{-2.6}$	$27.0^{+4.0}_{-3.1}$
BD projected separation	au	$0.20^{+0.03}_{-0.02}$	$22.3^{+2.4}_{-1.5}$

Only the NE models are shown, as we have ruled out the SE models. The relative proper motion of the lens and source was measured north (0°) to east (90°) and in the heliocentric frame. The projected and physical separations are defined at the time of the event. The minimum physical separation of the planet for scenario 1 (close NE) arises from stability requirements during the host star's MS phase.

post-common-envelope binaries^{29–31}. Models are able to explain these wider post-common-envelope binaries only if mass transfer was first initiated during the AGB phase of the progenitor of the WD, when its envelope is expected to be loosely bound and little gravitational energy is required to unbind it^{2,31,32}. Under this scenario, the BD's initial orbit around the MS host is expected to be 3–6 au (ref. 31). Nevertheless, even if this common-envelope evolution pathway remains valid for a substantially less massive BD, long-term orbital stability for the system (for example, ref. 33) would require the planet to be on an initially wide orbit ($d \gtrsim 10$ au), which is already disfavoured by the planet orbital model.

Given the combination of evidence against the close NE model, we conclude that the wide NE model (scenario 2 in Fig. 3) is the most favoured scenario, such that neither the planet nor the BD interacted with the WD progenitor. In this case, this system may provide a possible glimpse into the distant future of our Solar System. Although Venus will eventually be engulfed and Mars will most certainly survive, the final fate of the Earth remains uncertain and critically depends on the stellar-mass-loss rate during the solar red-giant-branch phase³⁴, which remains poorly constrained³⁵. Certain models predict that the Earth may be engulfed during the solar tip-red-giant-branch-phase due to tidal interactions and dynamical drag^{36,37}. Nevertheless, if Earth does indeed survive, then its orbit is expected to expand to around twice its

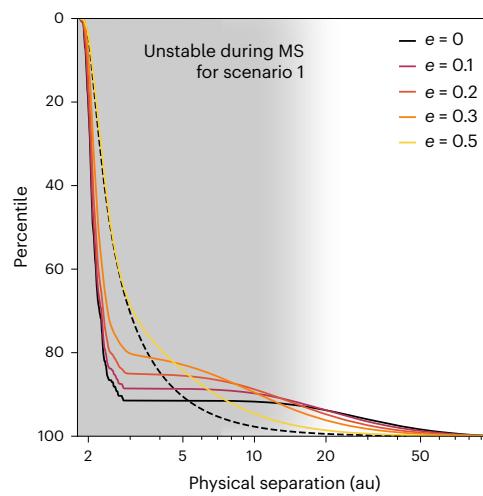


Fig. 2 | Planet's physical separation from the WD host during the peak of the event as inferred from its projected separation and the microlensing orbital motion. Cumulative distribution function for the marginal posterior distribution of the physical separation under a log-uniform prior is shown for different eccentricities. The difference between the close NE and wide NE models is minimal (Supplementary Figs. 2 and 3). Their mean values are displayed. The cumulative distribution function for the physical separation without the orbital motion constraints is shown for $e = 0$ (dashed line) for comparison. The shaded region indicates the planetary orbits that would have been initially unstable with the BD orbit during the host star's MS phase under the close NE model (scenario 1 in Fig. 3).

current size, comparable to the current orbit for KB200414Lb. Therefore, the Earth-mass planet KB200414Lb probably represents a similar yet more fortuitous future compared to that of our own planet Earth.

Methods

Observations

We observed the location of the planetary microlensing^{38,39} event KB200414 (ref. 1) using the wide mode of the NIRC2 camera on the Keck II telescope on 25 May 2023 (UT) under programme U152 (Primary Investigator J.S.B. and Science Primary Investigator K.Z.). The pixel scale was 0.04" per pixel with a 40" by 40" field of view. Five deep images were taken with 30 s of exposure per image for the relative photometry on the target. Two shallow images were taken, each with 10 s of total integration time, which consisted of 20 co-adds of 0.5 s exposures. The shallow image had a brighter saturation limit and was used for calibration to the VVV photometric system. The shallow and deep images were corrected for nonlinearity⁴⁰, sky-subtracted, flat-fielded and averaged into two master images.

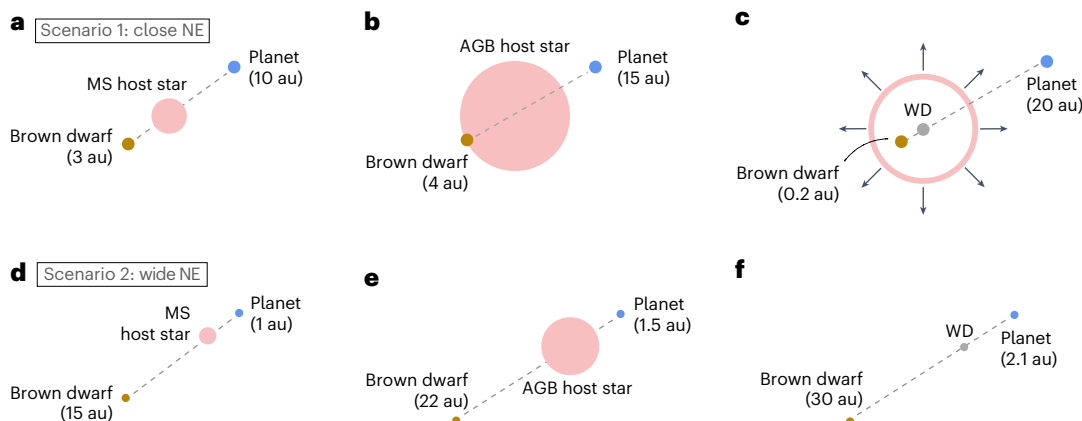


Fig. 3 | Illustration of the system's possible evolutionary histories under the close NE and wide NE models. **a–c**, Close NE model. **a**, Initial configuration, with a close-in BD and wide-orbit planet. **b**, The orbits expand due to host-star mass loss. The AGB host star overflows the Roche lobe. The BD enters the common envelope. **c**, The common envelope is ejected as the BD orbit reduces to 0.2 au.

The planetary orbit further expands. **d–f**, Wide NE model. **d**, Initial configuration, with a close-in planet and wide-orbit BD. **e**, The orbits expand due to host-star mass loss. Neither the BD nor the planet interact with the AGB host star. **f**, The orbits continue to expand. Objects and orbits are not drawn to scale. Separations are representative values.

We identified the target in the Keck image by transforming the magnified source location in the image taken by the Canada–France–Hawaii Telescope (CFHT; Fig. 1b) into the Keck frame. A linear transformation between the two frames was derived using ten reference stars listed in Supplementary Table 1, resulting in a residual standard error of 22.6 mas. We unequivocally identified the Keck star located at (502.43, 559.02) as the event location, which has a nominal offset from the CFHT source location of 22.0 ± 22.6 mas, that is, within one pixel in the Keck image.

We then performed aperture photometry with a radius of five pixels (0.2") on the two stacked images using the photutils package⁴¹. Eleven relatively isolated stars in the shallow image with $12.5 < K_{s,VVV} < 15.5$ were calibrated to VVV DR4 aperture photometry⁴², which resulted in a zero-point uncertainty of 0.03 mag. We then calibrated the deep image to the shallow image, which resulted in a calibrated target brightness of $K_s = 16.99 \pm 0.03$. Given the relative proper motion of the lens and source of ~ 8 mas yr⁻¹ (Table 2), we expected the lens–source separation to be ~ 24 mas at the time of the Keck observations, much smaller than the ~ 80 mas Keck point spread function. Therefore, the target flux includes the combined flux from the lens and source stars. Note that the OGLE blended light may be attributed to four stars within 0.5" to the west and north-west, which have a total brightness of $K_s \simeq 16.8$. This is comparable to the source star's brightness (see 'Flux constraints'), which is also the case for the OGLE *I*-band blend.

Flux constraints

The source star's brightness was measured only in the *V* and *I* bands and slightly differed across models. As the follow-up observations were performed in the K_s band, we first converted the *I*-band source brightness to the K_s band from its intrinsic ($I - K_s$) colour and reddening $E(I - K_s)$. To derive the extinction and reddening, we constructed a ($I - K_s$) versus K_s colour–magnitude diagram by cross-matching OGLE-III and VVV catalogue stars within 2' of KB200414 (Supplementary Fig. 1). The VVV photometry was calibrated to 2MASS. We measured the centroid of the red-giant clump as $(I - K_s, K_s)_{cl} = (2.49 \pm 0.01, 13.06 \pm 0.02)$. For the intrinsic centroid of the red-giant clump, we adopted $(I - K_s, K_s)_{cl,0} = (1.46 \pm 0.04, 12.89 \pm 0.04)$ (refs. 43,44), which implies $E(I - K_s) = 1.03 \pm 0.04$ and $A_{K_s} = 0.17 \pm 0.04$. We also cross-checked the K_s extinction in colour space. Using the OGLE extinction calculator, we derived reddening $E(V - I) = 0.972$ and $E(J - K_s) = 0.316$ (ref. 45) towards the sight line of KB200414. Adopting the extinction law of ref. 46, we have $A_{K_s} = 0.528E(J - K_s) = 0.17$, which is in agreement with the analysis of the colour–magnitude diagram.

We then derived the intrinsic ($I - K_s$) colour of the source from its intrinsic ($V - I$) colour, which was reported as $(V - I)_{s,0} = 0.84 \pm 0.03$ in ref. 1. Using colour–colour relations⁴⁷ and the zero-point offset from K_s to standard *K* of 0.04 mag (ref. 48), we derived $(I - K_s)_{s,0} = 1.06 \pm 0.04$ and, thus, $(I - K_s)_s = (I - K_s)_{s,0} + E(I - K_s) = 2.09 \pm 0.06$, which was used to convert the *I*-band source brightness (Table 4 of ref. 1) into the K_s source brightness listed in Table 1.

We derived the expected K_s brightness for hypothetical MS lenses using MESA⁴⁹ Isochrones and Stellar Tracks (MIST)^{50,51}. The apparent brightness depends on the mass, distance, age, metallicity and extinction experienced by the lens star. To rule out all possible MS lenses, we had to consider stellar properties that lead to the faintest brightness. Therefore, we adopted metal-rich isochrones ([Fe/H] = 0.5) and considered the faintest possible brightness for ages over 100 Myr and 10 Gyr.

The mass and distance of the primary lens star were derived from the angular Einstein radius and the microlensing parallax, as constrained by the light-curve models and source star's properties. We directly adopted the published light-curve models of ref. 1 in the form of raw Markov chain Monte Carlo chains. We searched for other degenerate models using a machine-learning algorithm^{52,53}, which did not yield new solutions but recovered the existing ones. Note that the lens properties originally reported in Table 5 of ref. 1 were based on a Galactic model that rejected parameter samples that would result in the MS lens being brighter than the blend flux of $I = 18.9$. As we rejected the hypothesis that the primary lens is an MS star, we simply adopted a uniform prior, which resulted in slightly different reported values.

The angular Einstein radius is defined as

$$\theta_E = \sqrt{\kappa M_L \pi_{rel}}, \quad (1)$$

where M_L is the mass of the lens, $\pi_{rel} = \pi_L - \pi_S$ is the lens–source relative parallax and

$$k = \frac{4G}{c^2 au} \simeq 8.144 \text{ mas}/M_\odot. \quad (2)$$

The microlensing parallax is defined as the lens–source relative parallax in units of the angular Einstein radius:

$$\pi_E = \frac{\pi_{rel}}{\theta_E} = \sqrt{\frac{\pi_{rel}}{\kappa M_L}}. \quad (3)$$

Therefore, the lens mass is $M_L = \theta_E / (\kappa \pi_E)$ and the lens parallax is $\pi_L = \pi_{rel} - \pi_S = \pi_E \theta_E - \pi_S$. For the source parallax, we adopted a source

distance of $D_s = 8.0 \pm 0.8$ kpc, which was derived using the triaxial G2 Galactic bulge model originally adapted in ref. 54 for microlensing population studies.

Following ref. 55, we derived the K_s extinction experienced by the lens star (regardless of whether it is an MS star or WD) as

$$A_{K_s}(D_L) = \int_0^{D_L} a_{K_s} \times n_d(D) dD, \quad (4)$$

where D_L is the lens distance, $n_d(D)$ is the dust density at distance D and a_{K_s} is the extinction in units of mag kpc⁻³ dust. We adopted an exponential Galactic dust distribution model where, in cylindrical coordinates,

$$n_d(D) \propto \exp\left(-\frac{|z(D)|}{z_d} - \frac{R(D)}{R_d}\right), \quad (5)$$

where the radial distance from the Galactic centre (R) and height above the Galactic plane (z) are related to the distance to the observer (D), and the Galactic longitude (l) and latitude (b) by

$$z(D) = z_\odot + D \sin b \simeq z_\odot + Db, \quad (6)$$

$$R(D) = \sqrt{(R_\odot - D \cos b \cos l)^2 + (D \cos b \sin l)^2} \simeq |R_\odot - D|. \quad (7)$$

In the above equations, the adopted dust length scales were $(R_d, z_d) = (3.2, 0.1)$ (ref. 56) and the adopted location of the Sun was $(R_\odot, z_\odot) = (8.3, 0.023)$ kpc (refs. 57,58). The extinction constant was derived as $a_{K_s} = 0.67$ by considering $A_{K_s}(D_s) = 0.17$ and $D_s = 8$ kpc. The minimum expected brightness for MS lenses consistent with the light-curve models is reported in Table 1, with K_s lens extinctions in the range 0.03–0.06 mag.

WD properties

The age of the Universe limits the lowest mass for a WD that formed through the evolution of a single star. CO WDs are known to have a mass distribution sharply centred around $0.59 M_\odot$, which drops off quickly for lower masses. Essentially, no WDs have been found with $M < 0.45 M_\odot$ except for ELM/helium WDs¹⁴. We, therefore, imposed a host-mass lower limit of $M > 0.45 M_\odot$ as a Bayesian prior to further refine the properties of the planetary system. As low-mass WDs ($\sim 0.5 M_\odot$) were already strongly favoured by the light-curve models, the inferred host mass was relatively insensitive to the specific WD mass prior adopted, provided that some form of prior was applied to reject the regime $M < 0.45 M_\odot$ where singular WDs are extremely uncommon.

We derived the expected K_s brightness of the CO WD for the two NE solutions using the isochrone for $0.54 M_\odot$ DA WDs under the BaSTI stellar evolution model⁵⁹. We considered the possible WD brightness under a uniform cooling age distribution from 0.1 to 10 Gyr. We applied the same extinction scheme as for MS lenses, which resulted in an expected WD lens brightness of $K_s \sim 24$. As such, it would be favourable to directly observe the WD lens at the first light of the 30-m-class telescopes (estimated 2030), which would separate it from the glare of the source star by around 80 mas. It may also be possible to detect the WD lens with the James Webb Space Telescope.

Orbital model

We inferred the planet's physical separation (d) and semimajor axis (a) from its projected separation (s) by leveraging the effect of the microlensing orbital motion, which was included in the light-curve models originally published by ref. 1. This approach considers the projected separation (s) and the relative angle (α) as changing linearly in time, which are parametrized as $(\dot{s}, \dot{\alpha})$. As the planetary light-curve feature

occurred during a short 7 d window, this linear parameterization is likely sufficient. We validated it by examining how much $(\dot{s}, \dot{\alpha})$ were actually predicted to change during this time frame.

We converted the planet's orbital motion parameters $(\dot{s}, \dot{\alpha})$ for the NE models to physical units under the host-mass lower limit, which were approximately $\dot{\alpha} = 0.3 \pm 0.1$ rad yr⁻¹ and $\dot{s} = 0.0 \pm 0.1$ au yr⁻¹ (Extended Data Table 1). Note that ref. 1 considered orbital motion only for the planet and not for the BD. They estimated that doing so would require an additional $\mathcal{O}(10^6)$ CPU hours for each degenerate model. Moreover, they suggested that incorporating the BD orbital motion would not make a pronounced impact on the light curve, as the light-curve anomaly associated with the BD is less than half a day in duration.

We considered an orbital model with six parameters: host mass (M), semimajor axis (a), eccentricity (e), inclination (i), argument of periaxis (ω) and the reference phase (ϕ_0), which is defined as the difference between the reference time (t_0) in the light-curve model and the time of periastron (t_{peri}), and normalized to the orbital period (P): $\phi_0 = (t_0 - t_{\text{peri}})/P$. This parametrization made the orbital model invariant to the orbital period and host mass, which we used to scale the orbital model as a separate step.

The physical separation and semimajor axis are deterministically related to the projected separation and orbital elements (e, i, ϕ_0, ω) through $d = s/f(\theta)$ and $a = s/g(\theta)$, where θ is a shorthand for the aforementioned orbital elements. We first transformed samples from the projected separation posterior (Table 2) into the physical separation posterior without considering the orbital motion constraints. To this end, we sampled a dense grid of orbital elements from a uniform prior for ω and ϕ_0 and a sine prior for i , which facilitated an isotropic prior on the orbital plane. We sampled distinct eccentricities over $[0, 0.5]$ for a step size of 0.1. We then evaluated a grid of transforming factors $f(\theta)$ and $g(\theta)$ from the grid of orbital elements using the exoplanet package⁶⁰. Finally, we acquired (M, s) samples from the light-curve posterior (Table 2) and applied the grid of transforming factors to derive samples of the physical separation. We then applied the same procedure to the semimajor axis.

Formally, we applied a change of variables for which the physical separation posterior was related to the projected separation posterior (from the light-curve model) through

$$p(d, \theta) = p(s, \theta) \left| \frac{\partial s}{\partial d} \right| = p(s, \theta) f(\theta) = p(s, \theta) \frac{s}{d}, \quad (8)$$

where $p(s, \theta)$ is a shorthand for $p(s = f(\theta)d, \theta)$. From the above equation, we can interpret $p(d, \theta)$ as a posterior distribution, where $p(s, \theta)$ is the (partial) likelihood of the projected separation. The physical separation prior is given by $p(d) \simeq 1/d$, namely a log-uniform distribution. We verified the log-uniform prior numerically given its importance in interpreting the final results.

We can write the above intermediate posterior as $p(d, \theta|s)$, as it accounts only for the projected separation measurement and not the orbital motion measurements. Observe that the full (taking into account all of s, \dot{s} and $\dot{\alpha}$) and intermediate posteriors follows the same joint distribution $p(d, \theta, s, \dot{s}, \dot{\alpha})$:

$$p(d, \theta|s, \dot{s}, \dot{\alpha}) \propto p(d, \theta, s, \dot{s}, \dot{\alpha}) \propto p(d, \theta|s)p(\dot{s}, \dot{\alpha}|M, s, \theta). \quad (9)$$

Therefore, we can convert samples from the intermediate posterior to the full posterior with an importance weight of $p(\dot{s}, \dot{\alpha}|M, s, \theta)$, namely the partial likelihood of the orbital motion constraints. The predicted orbital motion was derived using the finite difference on the aforementioned orbital element grid, which requires knowledge of the orbital period. The host mass associated with the projected separation (the M and s samples from Table 2) underlying each parameter combination was used to derive the orbital period from Kepler's third

law. Therefore, our approach natively accounts for the covariance between M and s , which circumvents the difficulty that s is an observable whereas M is a model parameter. Therefore, we expect this approach to be useful for similar microlensing orbital analysis in the future.

We validated the assumption of linear orbital motion by examining the extent to which $(\dot{s}, \dot{\alpha})$ are predicted to change during the planetary light-curve feature. We found that they changed by merely $\mathcal{O}(10^{-3})$ au yr $^{-1}$ and $\mathcal{O}(10^{-5})$ rad yr $^{-1}$, which implies that linear orbital motion is a sufficient parametrization.

As we discuss in the main text, the bimodality of the physical separation represents two distinct regions of orbital space that are allowed under the orbital model. Extended Data Fig. 1 visualizes the marginal likelihood $p(\dot{s}, \dot{\alpha}|i, \phi_0)$ for the inclination and reference phase under different eccentricities. To ease interpretation and without substantial loss of generality for mildly eccentric orbits, we fixed the argument of periapsis to $\omega = \pi/2$ such that periastron and apastron occur at conjunction. We can see that the planet is either near greatest elongation in an inclined orbit or near conjunction on a nearly edge-on orbit, with the former substantially favoured.

To interpret the origins of this degeneracy (bimodality), observe that if the planet were on a circular, face-on orbit, then given $a \simeq 2.1$ au and $M \simeq 0.5 M_{\odot}$, we would expect a constant $\dot{\alpha} \simeq 1.5$ rad yr $^{-1}$ from Kepler's third law, which is much greater than the measured $\dot{\alpha} \simeq 0.3$ rad yr $^{-1}$. Therefore, the orbit must be substantially inclined. Furthermore, the measured \dot{s} is close to zero, which indicates that the planet is either near conjunction or longest elongation, which are the two locations where the projected separation remains stationary. If the planet were near conjunction, then its physical separation would greatly exceed the projected separation, which leads to a much longer orbital period that serves to reduce $\dot{\alpha}$. This also explains why the conjunction scenario is favoured at apastron (Extended Data Fig. 1), where the planet's angular velocity is also intrinsically smaller.

Data availability

The reduced Keck images are available via Zenodo at <https://doi.org/10.5281/zenodo.13128167> (ref. 61). The raw data will be available on the Keck Observatory Archive (<https://koa.ipac.caltech.edu/>) after the 18-month proprietary period.

References

1. Zang, W. et al. An Earth-mass planet in a time of COVID-19: KMT-2020-BLG-0414Lb. *Res. Astron. Astrophys.* **21**, 239 (2021).
2. Dominik, M. The binary gravitational lens and its extreme cases. *Astron. Astrophys.* **349**, 108–125 (1999).
3. Jiang, G. et al. OGLE-2003-BLG-238: microlensing mass estimate of an isolated star. *Astrophys. J.* **617**, 1307 (2004).
4. Poindexter, S. et al. Systematic analysis of 22 microlensing parallax candidates. *Astrophys. J.* **633**, 914 (2005).
5. Wizinowich, P. L. et al. The W. M. Keck Observatory laser guide star adaptive optics system: overview. *Publ. Astron. Soc. Pac.* **118**, 297–309 (2006).
6. van Dam, M. A. et al. The W. M. Keck Observatory laser guide star adaptive optics system: performance characterization. *Publ. Astron. Soc. Pac.* **118**, 310–318 (2006).
7. Brown, W. R. et al. The ELM survey. VIII. Ninety-eight double white dwarf binaries. *Astrophys. J.* **889**, 49 (2020).
8. Brown, W. R., Kilic, M., Kosakowski, A. & Gianninas, A. The ELM Survey. IX. A complete sample of low-mass white dwarf binaries in the SDSS footprint. *Astrophys. J.* **933**, 94 (2022).
9. Sun, M. & Arras, P. Formation of extremely low-mass white dwarf binaries. *Astrophys. J.* **858**, 14 (2018).
10. Li, Z., Chen, X., Chen, H.-L. & Han, Z. Formation of extremely low-mass white dwarfs in double degenerates. *Astrophys. J.* **871**, 148 (2019).
11. Zorotovic, M., Schreiber, M. R., Gänsicke, B. T. & Nebot Gómez-Morán, A. Post-common-envelope binaries from SDSS. IX. Constraining the common-envelope efficiency. *Astron. Astrophys.* **520**, A86 (2010).
12. Belloni, D., Zorotovic, M., Schreiber, M. R., Parsons, S. G. & Garbutt, J. A. Formation of long-period post-common-envelope binaries. I. No extra energy is needed to explain oxygen-neon white dwarfs paired with AFGK-type main-sequence stars. *Astron. Astrophys.* **686**, A61 (2024).
13. Falcon, R. E., Winget, D. E., Montgomery, M. H. & Williams, K. A. A gravitational redshift determination of the mean mass of white dwarfs. DA stars. *Astrophys. J.* **712**, 585–595 (2010).
14. Kilic, M. et al. The 100 pc white dwarf sample in the SDSS footprint. *Astrophys. J.* **898**, 84 (2020).
15. Chen, J. & Kipping, D. Probabilistic forecasting of the masses and radii of other worlds. *Astrophys. J.* **834**, 17 (2016).
16. Otegi, J. F., Bouchy, F. & Helled, R. Revisited mass-radius relations for exoplanets below $120 M_{\oplus}$. *Astron. Astrophys.* **634**, A43 (2020).
17. Cummings, J. D., Kalirai, J. S., Tremblay, P.-E., Ramirez-Ruiz, E. & Choi, J. The white dwarf initial-final mass relation for progenitor stars from 0.85 to $7.5 M_{\odot}$. *Astrophys. J.* **866**, 21 (2018).
18. Dong, S. et al. Microlensing event MOA-2007-BLG-400: exhume the buried signature of a cool, Jovian-mass planet. *Astrophys. J.* **698**, 1826–1837 (2009).
19. Skowron, J. et al. Binary microlensing event OGLE-2009-BLG-020 gives verifiable mass, distance, and orbit predictions. *Astrophys. J.* **738**, 87 (2011).
20. Jackson, B., Greenberg, R. & Barnes, R. Tidal evolution of close-in extrasolar planets. *Astrophys. J.* **678**, 1396 (2008).
21. Jones, M. I., Jenkins, J. S., Bluhm, P., Rojo, P. & Melo, C. H. F. The properties of planets around giant stars. *Astron. Astrophys.* **566**, A113 (2014).
22. Kass, R. E. & Raftery, A. E. Bayes factors. *J. Am. Stat. Assoc.* **90**, 773–795 (1995).
23. Ida, S. & Lin, D. N. C. Toward a deterministic model of planetary formation. I. A desert in the mass and semimajor axis distributions of extrasolar planets. *Astrophys. J.* **604**, 388 (2004).
24. Rasio, F. A. & Ford, E. B. Dynamical instabilities and the formation of extrasolar planetary systems. *Science* **274**, 954–956 (1996).
25. Gould, A. et al. Free-floating planets, the Einstein desert, and 'Oumuamua. *J. Korean Astron. Soc.* **55**, 173–194 (2022).
26. Sumi, T. et al. Free-floating planet mass function from MOA-II 9-year survey towards the Galactic bulge. *Astron. J.* **166**, 108 (2023).
27. Mróz, P., Ban, M., Marty, P. & Poleski, R. Free-floating or wide-orbit? Keck adaptive-optics observations reveal no host stars near free-floating planet candidates. *Astron. J.* **167**, 40 (2023).
28. Nelson, L., Schwab, J., Ristic, M. & Rappaport, S. Minimum orbital period of precataclysmic variables. *Astrophys. J.* **866**, 88 (2018).
29. Kruse, E. & Agol, E. KOI-3278: a self-lensing binary star system. *Science* **344**, 275–277 (2014).
30. Kawahara, H. et al. Discovery of three self-lensing binaries from Kepler. *Astron. J.* **155**, 144 (2018).
31. Yamaguchi, N. et al. Wide post-common envelope binaries containing ultramassive white dwarfs: evidence for efficient envelope ejection in massive asymptotic giant branch stars. *Mon. Not. R. Astron. Soc.* **527**, 11719–11739 (2024).
32. Izzard, R. G. & Jermyn, A. S. Post-AGB discs from common-envelope evolution. *Galaxies* **6**, 97 (2018).
33. Deck, K. M., Payne, M. & Holman, M. J. First-order resonance overlap and the stability of close two-planet systems. *Astrophys. J.* **774**, 129 (2013).
34. Guo, J., Lin, L., Bai, C. & Liu, J. The effects of solar Reimers' η on the final destinies of Venus, the Earth, and Mars. *Astrophys. Space Sci.* **361**, 122 (2016).

35. McDonald, I. & Zijlstra, A. A. Mass-loss on the red giant branch: the value and metallicity dependence of Reimers' η in globular clusters. *Mon. Not. R. Astron. Soc.* **448**, 502–521 (2015).

36. Schröder, K.-P. & Connon Smith, R. Distant future of the Sun and Earth revisited. *Mon. Not. R. Astron. Soc.* **386**, 155–163 (2008).

37. Lanza, A. F., Lebreton, Y. & Sallard, C. Residual eccentricity of an Earth-like planet orbiting a red giant Sun. *Astron. Astrophys.* **674**, A176 (2023).

38. Mao, S. & Paczyński, B. Gravitational microlensing by double stars and planetary systems. *Astrophys. J.* **374**, L37 (1991).

39. Gould, A. & Loeb, A. Discovering planetary systems through gravitational microlenses. *Astrophys. J.* **396**, 104–114 (1992).

40. Metchev, S. A. & Hillenbrand, L. A. The Palomar/Keck adaptive optics survey of young solar analogs: evidence for a universal companion mass function. *Astrophys. J. Suppl. Ser.* **181**, 62 (2009).

41. Bradley, L. et al. astropy/photutils: 1.5.0. Zenodo <https://doi.org/10.5281/zenodo.10967176> (2022).

42. Minniti, D. et al. VISTA variables in the Via Lactea (VVV): the public ESO near-IR variability survey of the Milky Way. *New Astron.* **15**, 433–443 (2010).

43. Nataf, D. M. et al. Reddening and extinction toward the Galactic bulge from Ogle-III: the inner Milky Way's RV ~2.5 extinction curve. *Astrophys. J.* **769**, 88 (2013).

44. Nataf, D. M. et al. Interstellar extinction curve variations towards the inner Milky Way: a challenge to observational cosmology. *Mon. Not. R. Astron. Soc.* **456**, 2692–2706 (2016).

45. Gonzalez, O. A. et al. Reddening and metallicity maps of the Milky Way bulge from VVV and 2MASS. II. The complete high resolution extinction map and implications for Galactic bulge studies. *Astron. Astrophys.* **543**, A13 (2012).

46. Nishiyama, S. et al. Interstellar extinction law toward the Galactic Center. III. J, H, KS bands in the 2MASS and the MKO systems, and 3.6, 4.5, 5.8, 8.0 μ m in the Spitzer/IRAC system. *Astrophys. J.* **696**, 1407 (2009).

47. Bessell, M. S. & Brett, J. M. JHKLM photometry: standard systems, passbands, and intrinsic colors. *Publ. Astron. Soc. Pac.* **100**, 1134 (1988).

48. Carpenter, J. M. Color transformations for the 2MASS second incremental data release. *Astron. J.* **121**, 2851–2871 (2001).

49. Paxton, B. et al. Modules for Experiments in Stellar Astrophysics (MESA). *Astrophys. J. Suppl. Ser.* **192**, 3 (2011).

50. Choi, J. et al. Mesa Isochrones and Stellar Tracks (MIST). I. Solar-scaled models. *Astrophys. J.* **823**, 102 (2016).

51. Dotter, A. MESA Isochrones and Stellar Tracks (MIST). O. methods for the construction of stellar isochrones. *Astrophys. J. Suppl. Ser.* **222**, 8 (2016).

52. Zhang, K. et al. Real-time likelihood-free inference of roman binary microlensing events with amortized neural posterior estimation. *Astron. J.* **161**, 262 (2021).

53. Zhang, K., Gaudi, B. S. & Bloom, J. S. A ubiquitous unifying degeneracy in two-body microlensing systems. *Nat. Astron.* **6**, 782–787 (2022).

54. Zhu, W. et al. Toward a Galactic distribution of planets. I. Methodology and planet sensitivities of the 2015 high-cadence Spitzer microlens sample. *Astron. J.* **154**, 210 (2017).

55. Yang, H. et al. KMT-2021-BLG-0171Lb and KMT-2021-BLG-1689Lb: two microlensing planets in the KMTNet high-cadence fields with followup observations. *Mon. Not. R. Astron. Soc.* **516**, 1894–1909 (2022).

56. Li, L. et al. Three-dimensional structure of the Milky Way dust: modeling of LAMOST data. *Astrophys. J.* **858**, 75 (2018).

57. Gillessen, S. et al. Monitoring stellar orbits around the massive black hole in the Galactic Center. *Astrophys. J.* **692**, 1075 (2009).

58. Maíz-Apellániz, J. The spatial distribution of O-B5 stars in the solar neighborhood as measured by Hipparcos. *Astron. J.* **121**, 2737 (2001).

59. Salaris, M., Cassisi, S., Pietrinferni, A., Kowalski, P. M. & Isern, J. A large stellar evolution database for population synthesis studies. VI. White dwarf cooling sequences. *Astrophys. J.* **716**, 1241 (2010).

60. Foreman-Mackey, D. et al. exoplanet: gradient-based probabilistic inference for exoplanet data & other astronomical time series. *J. Open Source Softw.* **6**, 3285 (2021).

61. Zhang, K. Reduced Keck images for KMT-2020-BLG-0414. Zenodo <https://doi.org/10.5281/zenodo.13128167> (2024).

Acknowledgements

K.Z. is supported by the Eric and Wendy Schmidt AI in Science Postdoctoral Fellowship, a Schmidt Futures programme. K.Z. and J.S.B. were partially supported by the Gordon and Betty Moore Foundation and a grant from the National Science Foundation (Award No. 2206744). W.Z. acknowledges support from the Harvard-Smithsonian Center for Astrophysics through a fellowship. W.Z. and S.M. acknowledge support from the National Natural Science Foundation of China (Grant No. 12133005). J.R.L. acknowledges support from the National Science Foundation (Grant No. 1909641) and the Heising-Simons Foundation (Grant No. 2022-3542). K.Z. thanks M. He for assistance on an initial version of the cover art proposal. W.Z. thanks H. Wang for fruitful discussions on the Keck proposal. This research has made use of the KMTNet system operated by the Korea Astronomy and Space Science Institute. The data were obtained at three host sites, namely the Cerro Tololo Inter-American Observatory in Chile, the South African Astronomical Observatory in South Africa and the Siding Spring Observatory in Australia. Data transfer from a host site to the Korea Astronomy and Space Science Institute was supported by the Korea Research Environment Open Network. Some of the data presented herein were obtained at Keck Observatory, which is a private 501(c)3 non-profit organization operated as a scientific partnership among the California Institute of Technology, the University of California and the National Aeronautics and Space Administration (NASA). The observatory was made possible by the generous financial support of the W. M. Keck Foundation. We recognize and acknowledge the very significant cultural role and reverence that the summit of Mauna Kea has always had within the Native Hawaiian community. We are most fortunate to have had the opportunity to conduct observations from this mountain. This research uses data obtained through the Telescope Access Program, which was funded by member institutes and was partly based on observations obtained with MegaPrime/MegaCam, a joint project of CFHT and DAPNIA, which is a part of the French Alternative Energies and Atomic Energy Commission, at the CFHT, which is operated by the National Research Council of Canada, the Institut National des Sciences de l'Univers of the French National Centre for Scientific Research and the University of Hawaii. The observations at the CFHT were performed with care and respect at the summit of Mauna Kea, which is a significant cultural and historic site.

Author contributions

K.Z. reduced the Keck data, developed the probabilistic framework for inferring the planet's physical separation, led the overall analysis and interpretation, and wrote the paper. K.Z., K.E.-B. and E.A. developed the interpretation of the system's evolutionary history. K.Z. and W.Z. conceived of the observations and led the writing of the Keck proposal. W.Z. contributed to the extinction and lens light analysis. K.Z. and J.S.B. obtained the observing time as the Science PI and PI of Keck programme U152. J.R.L., S.T., J.S.B. and N.L. contributed to the observing. All co-authors participated in discussions and contributed to the revision of the paper.

Competing interests

The authors declare no competing interests.

Additional information

Extended data is available for this paper at
<https://doi.org/10.1038/s41550-024-02375-9>.

Supplementary information The online version contains supplementary material available at <https://doi.org/10.1038/s41550-024-02375-9>.

Correspondence and requests for materials should be addressed to Keming Zhang or Weicheng Zang.

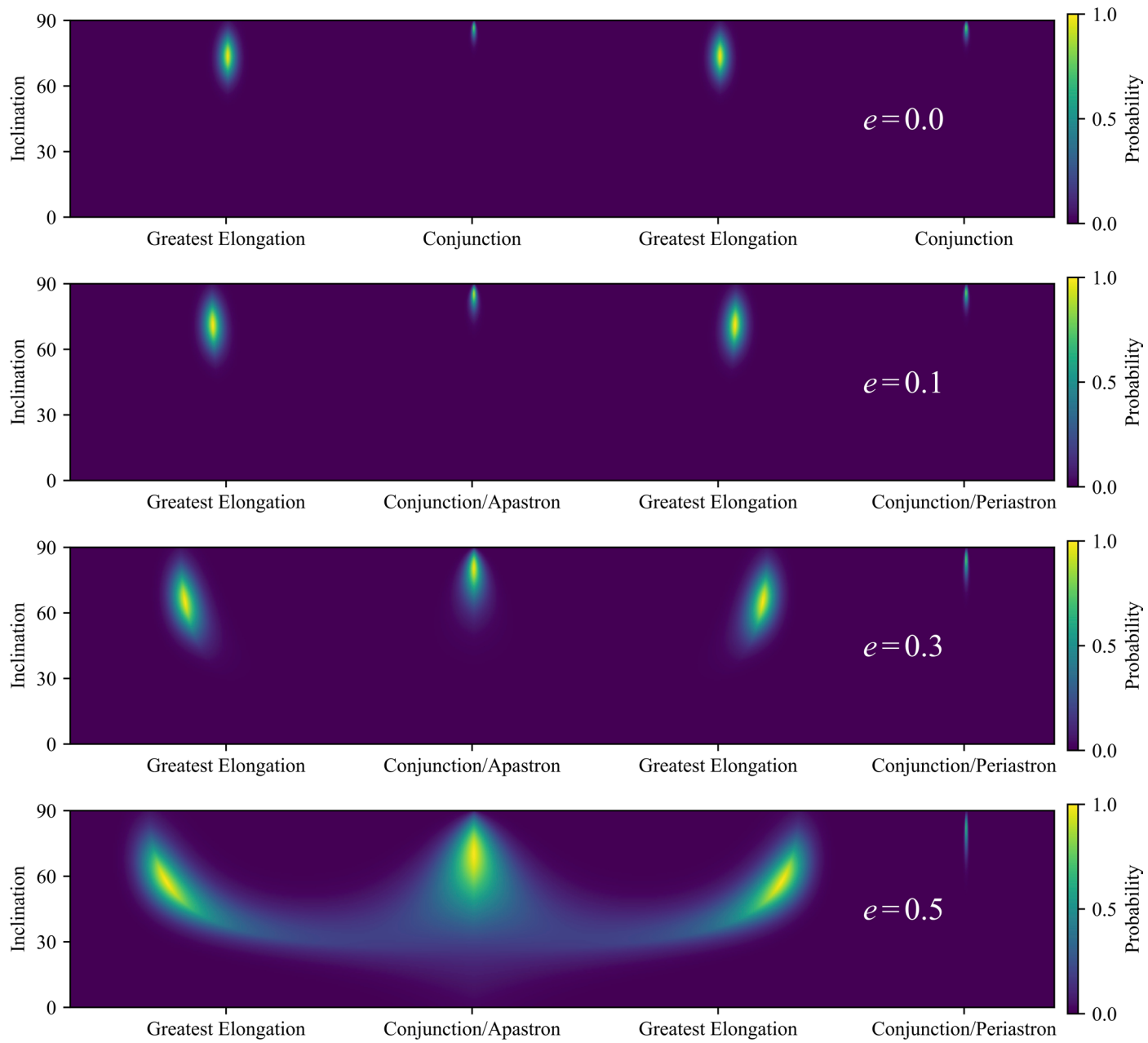
Peer review information *Nature Astronomy* thanks the anonymous reviewers for their contribution to the peer review of this work.

Reprints and permissions information is available at www.nature.com/reprints.

Publisher's note Springer Nature remains neutral with regard to jurisdictional claims in published maps and institutional affiliations.

Springer Nature or its licensor (e.g. a society or other partner) holds exclusive rights to this article under a publishing agreement with the author(s) or other rightsholder(s); author self-archiving of the accepted manuscript version of this article is solely governed by the terms of such publishing agreement and applicable law.

© The Author(s), under exclusive licence to Springer Nature Limited 2024



Extended Data Fig. 1 | Marginal likelihood for the inclination and orbital phase for different assumed eccentricities. Shown for the special case of $\omega = \pm \pi/2$ where apastron and periastron are aligned with conjunction for eccentric orbits.

Extended Data Table 1 | Orbital motion parameters for the NE models

	Close-NE	Wide-NE
$\dot{\alpha}$ (rad yr ⁻¹)	0.30 ± 0.15	0.27 ± 0.11
\dot{s} (au yr ⁻¹)	0.00 ± 0.13	-0.08 ± 0.15

Converted to physical units under the WD mass prior ($M > 0.45M_{\odot}$) and shown as the mean values and standard deviations of the respective posterior distribution.